In vitro evaluation of the antithyroid cancer properties of Y_2O_3/AgO nanocomposite produced through plasma-assisted eco-friendly technique using Solanum melongena L.

Youser Qasim Matroud
Al-Nahrain University
Rasha S. Ahmed
Al-Nahrain University
Raghad S. Mohammed
raghad.almaliki@uomustansiriyah.edu.iq

Mustansiriyah University

Research Article

Keywords: Plasma jet, Thyroid cancer, Anticancer activity, Yttrium, Green synthesis, FTIR

Posted Date: May 15th, 2026

DOI: https://doi.org/10.21203/rs.3.rs-9186037/v1

Additional Declarations: No competing interests reported.

In vitro evaluation of the antithyroid cancer properties of Y_2O_3/AgO nanocomposite produced through plasma-assisted eco-friendly technique using *Solanum melongena L.*

Youser Qasim Matroud[1], Rasha S. Ahmed[2], Raghad S. Mohammed[3*]

[1, 2]Department of Physiology, College of Medicine, Al-Nahrain University, Baghdad, Iraq

[3]Department of Physics, College of Science, Mustansiriyah University, Baghdad, 14022, Iraq.
*Correspondence: Email: raghad.almaliki@uomustansiriyah.edu.iq
ORCID: https://orcid.org/0000-0001-6164-6735

Abstract

Thyroid cancer is among the most common endocrine malignancies. Many anticancer drugs are ineffective for thyroid cancer, showing a significant need in order to identify new and effective treatment options. In the present study, an innovative and environmentally friendly method employing plasma-solution interaction with an extract of eggplant peel (*Solanum melongena L.*) as a reducing and stabilizing reagent was proposed for the synthesis of Y_2O_3/AgO nanocomposite, and its anticancer potentialities on B-CPA thyroid cancer cells are reported invitro. The Y_2O_3/AgO Nanocomposite was characterized through various techniques such as X-ray diffraction (XRD), energy dispersive X-ray spectroscopy (EDS), Fourier transform infrared spectrometry FTIR, field emission scanning electron microscope FE-SEM, transmission electron microscopy TEM and ultraviolet UV – visible. The XRD patterns of Y_2O_3/AgO NCs indicated that the samples are crystallized with an average crystal size of 9.82 nm. The EDX spectrum further confirmed the purity of the prepared Y_2O_3/AgO NCs. FE-SEM indicates that the Y_2O_3/AgO NCs have quasi-spherical morphologies, with a well-defined particle distribution on the surface. TEM verified the success of the plasma method in fabricating spherical Y_2O_3/AgO NCs with an average size of 3.7 ± 1.276 nm. The surface chemical composition and stabilization of Y_2O_3/AgO NCs were inferred through FT-IR. The UV–Vis spectrum exhibits a strong and broad peak at 319 nm indicating high absorption in this region with an energy band gap of 4.01 eV for the Y_2O_3/AgO NCs. According to a cytotoxicity test, the IC_{50} value of the Nthy-ori 3-1 normal cell line was 30.78 µg/mL. It is worth mentioning that Y_2O_3/AgO NCs exhibit much higher anticancer activity over the human thyroid cancer cells (B-CPAP) with an IC_{50} value of 16.14 µg/mL. To the best of our knowledge, this investigation is the first report on data analysis of the efficient implementation of plasma-solution reaction in extracts derived from eggplant (*Solanum melongena L.*) peel for the synthesis of Y_2O_3/AgO NCs as potential agents against thyroid cancer.

Keywords: Plasma jet, Thyroid cancer, Anticancer activity, Yttrium, Green synthesis, FTIR.

1. Introduction

Cancer is a collection of diseases in which abnormal cells divide without control and are able to invade other tissues[1]. It is the second most common cause of death, and its rising burden has a profound impact on patients and healthcare systems [2]. In 2022, the number of new cancer cases and deaths was estimated to be approximately 20 million and 9.7 million, respectively, at the global level, and represents one of the main challenges in public

health according to IARC/WHO [3]. A total of 821,214 new cases with thyroid cancer (TC) and 47,507 deaths were reported, with thyroid cancer (TC) appearing to be the most common endocrine malignancy [4]. TC represents about 4.1% of all cancer diagnoses and significantly affects women, being three to four times more prevalent in females than in males [5]. TC originates from follicular or parafollicular cells, including follicular, poorly differentiated, papillary thyroid carcinoma (PTC), and anaplastic thyroid carcinoma (ATC). PTC is responsible for 75-85% of the cases, whereas 95% of thyroid tumours are well or poorly differentiated[6]. Environmental risk factors, including radiation and iodine exposure as well as obesity, are implicated in increased thyroid cancer risk [7]. Typical treatments for cancer, including radiotherapy and chemotherapy, encounter some serious problems such as severe side effects, drug resistance, and very poor selectivity to the cancerous cells [8].

Cancer therapy is benefiting greatly from nanotechnology, in which drugs are enhanced for efficacy and, at the same time, side effects are reduced by improved drug-delivery techniques [9]. The solubility, stability, or bioavailability of drugs have been improved by researchers via a number of nanoparticle systems, including liposomes, polymer-based nanoparticles, and inorganic nanoparticles [10]. Furthermore, new nanodevices enable the controlled release of medication in response to physiological changes and improve therapeutic efficacy [11]. Additionally, nanotechnology can be added to theragnostics, since it combines tumor identification with site-specific therapeutic approaches through adapted material functionalization[12]. Nanomaterials, with diameters ranging from 1 to 100 nm [13], have particular physicochemical properties that make them suitable for different medical purposes such as diagnostics, tissue regeneration, and targeted drug delivery [14]. In oncology, they increase treatment efficacy in chemotherapy, radiotherapy, and surgery [15]. They are defined based on size, shape, and chemical properties [16], with attention, particularly being given to metal oxide nanoparticles [17], which have therapeutic effects including antimicrobial, antioxidative, anti-inflammatory, anticancer, and antidiabetic activities that could be useful alternatives for non-communicable disease treatment in view of safety issues of currently employed treatments [18].

Bimetallic oxide nanoparticles, made of two oxidized metals, show enhanced catalytic performance over monometallic nanoparticles because of their metal ratios and unique composition [19,20]. They benefit from synergistic effects, which will improve catalytic, and they possess unique magnetic, electrical, and optical properties [21]. These nanoparticles can be used in various domains, such as electrocatalysis, biosensing, adsorption, and drug delivery, because of their enhanced active sites and eco-friendly behavior [20]. Silver oxide (AgO) nanoparticles also show such characteristics as small size, large surface area, and bioactivity; hence, they may have potential application in therapeutic advancements [22]. These nanoparticles have notable antioxidant and anti-inflammatory activities, which could also be considered for the treatment of oxidative stress [23]. The silver oxide nanoparticles are stable, and their release of silver ions is regulated for targeted therapy [24]. Yttrium oxide (Y_2O_3), a rare earth metal oxide, can be prepared in many ways[25]and possesses characteristics such as a high dielectric constant, a wide band gap of about 5.8 eV, and outstanding chemical stability, which make it attractive for bio-applications, including drug delivery and gene therapy [26]. Y_2O_3 NPs have high luminescence efficiency and free radical elimination, but they are not widely used in nanomedicine. Antibacterial property and thermal stability make them promising for the treatment of cancer and neurological disorders [27].

Furthermore, the green synthesis of NPs using plant extract as a natural resource has revolutionized the production of NPs. provide sustainable applications by using natural resources and minimizing toxic substances [28]. This process employs flavonoids, alkaloids, and polyphenols as reducing and stabilizing agents for precursor ions [29,30]. Extracts from *Solanum melongena L.* peel are found to be rich in flavonoid and phenolic contents, which facilitate the preparation of nanoparticles and serve as natural antioxidants against diseases, including cancer [31]. Conventional approaches to synthesizing metallic nanoparticles are expensive and toxic, therefore attention has shifted towards their green variation thus involving environmentally sustainable solvents and renewable resources [32]. Biological sources are preferred due to their low cost and biocompatible nature [33]. While chemical methods offer greater control of nanoparticle properties, they may involve hazardous materials. In comparison, the like physical methods are more eco-friendly but less accurate [34]. The in-liquid plasma technique based on electric discharge between two electrodes in a dielectric liquid is known to generate customizable eco-friendly nanoparticles with the variation of experimental conditions [35,36]. The main advantage of plasma lies in its ability to generate reactive species in a solution, which can cause the reduced ions to deposit as nanoparticles without harmful chemicals [37]. By optimising the plasma solution reaction at different processing time and parameters allows for a straightforward experimental setup, including various electrodes and flow systems, making it ideal for mass production [38,39].

There is a lack of knowledge about the synthesis of Y_2O_3/AgO nanocomposite by plasma-assisted reduction with the extract of *Solanum melongena L. peel* and biomedical applications. Thus, this study aims to employ a novel, unique, environmentally friendly approach based on the plasma technique with eggplant peel extract for synthesizing Y_2O_3/AgO nanocomposites and analyzing their physical properties and evaluating their anti-cancer activity on thyroid cells. This hybrid plasma-solution interaction method that uses the extract makes it easy to quickly make nanoparticles using bioactive chemicals. This makes them more stable and purer while having less of an effect on the environment.

2. Materials and Method

2.1. Materials

Fresh peels of eggplant (*Solanum melongena L.*) were used as a natural source to prepare a plant extract. Yttrium nitrate [Y $(NO_3)_3$] and Silver nitrate ($AgNO_3$) were used as the metal precursor for nanoparticle synthesis, and absolute ethanol (96%) was acquired from a recognized chemical source. Deionized water was used throughout the experiments. Argon gas of 99.99% purity is used as the working gas for plasma generation.

2.2. Preparation of *Solanum melongena L. extract*

Fresh eggplants (*Solanum melongena L.*) have been purchased from a local market, thoroughly cleaned using tap water, peeled, and the skins were cut into small pieces. The samples were air-dried at atmospheric conditions for three days, and thereafter, crushed into a fine powder. Dissolve 2 g of the powder in 20 ml of 96% ethanol, stir magnetically for 30 minutes, then filter through filter paper. The resultant extract comprises flavonoids, polyphenols, and other phytochemical substances used as reducing and stabilizing agents for nanoparticles. As explained in Fig.1.

Fig. 1 A schematic revealed the steps of the preparation of an extract from eggplant peels created by BioRender.com.

2.3. Setup of the plasma system.

The experimental configuration of the plasma system used in this work is shown in Fig. 2a and comprises a DC high-voltage power source (3.5 kV) linked to two electrodes. The first electrode, a hollow copper electrode, functioned as the cathode for the passage of argon gas. The second electrode, a stainless-steel electrode which functioned as the anode, was immersed in a glass beaker filled with yttrium nitrate, silver nitrate solution and *Solanum melongena L.* peel extract. Argon gas with a purity of 99.99% was delivered at a flow rate of 2.5 L/min as measured by a flowmeter. Under these conditions, a steady plasma discharge was produced, resulting in a plasma plume that is 3 cm long. The solution and extract were exposed to plasma discharge for 15 minutes to facilitate nanoparticle synthesis.

2.4. Synthesis of Y_2O_3/AgO nanocomposite by hybrid method.

This research used a hybrid synthesis methodology, combining an eco-friendly biological technology with a plasma-solution interaction process. Such a hybrid strategy presents green approach of nanoparticle synthesis using waste plant materials like eggplant peels and turns waste agricultural by products as useful precursor towards nanomaterial fabrication. Firstly, a 0.05 M solution of Y_2O_3/AgO NCs was prepared from the dissolution process of 0.275 g yttrium nitrate ($Y(NO_3)_3$ in 20 mL deionized water with stirring on a magnetic stirrer for 10 min till the clear and homogenous solutions was achieved. Meanwhile, 0.17 g of silver nitrate ($AgNO_3$) was dissolved in 20 mL deionized water under the same conditions to get another transparent solution. Then, 10 mL each of yttrium nitrate and silver nitrate solutions were added to a 1-mL-volume *Solanum melongena L.* peel extract. Stir well to obtain a homogeneous mixture. The resulting mixture was then exposed to plasma discharge in 99.99% argon gas for 15 minutes, utilizing a plasma-solution interaction apparatus. As shown in Fig. 2a, the color of the solution gradually changed during plasma treatment, which proves Y_2O_3/AgO NCs success synthesis. The solution was transferred in to clean test tubes and kept for further analysis, as shown in Fig. 2b.

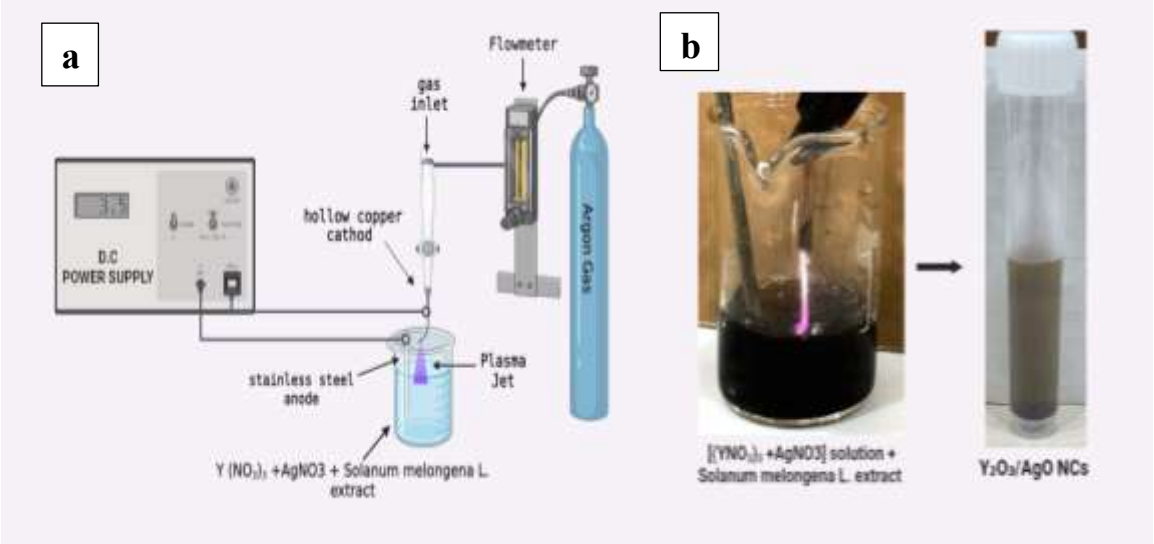

Fig. 2 (a): Schematic diagram of setup of the plasma system created by created by BioRender.com. **(b):** Real images.

2.5. Characterization of nanocomposite.

To verify the successful synthesis of Y_2O_3/AgO nanocomposite via plasma-assisted approach utilizing the extract of *Solanum melongena L.* peel, various complementary characterization techniques were employed. These techniques provided a thorough understanding of the structural, morphological, and optical properties of the synthesized nanoparticles, including XRD, UV-Vis, EDX, FTIR, FE-SEM, and TEM. The measurements were performed utilizing a PANalytical 021-44862778, Philips PW1730 X-ray diffractometer. EDS (VEGA3 TESCN). FE-SEM (MIRA2 TESCAN) operating at a voltage of 15.00 kilovolts (kV). The UV-Vis absorption spectra were obtained with a UV-Vis spectrometer.

2.6. Culture of cancer cells.

The BPC1 thyroid cancer cell line was supplied by the Iraqi Centre for Cancer Research and Medical Genetics for cell culture purposes. Thyroid cancer cells (BPC1) were inoculated in Dulbecco's modified Eagle's medium (DMEM) supplemented with 10% fetal bovine serum and 1% antibiotics (penicillin, streptomycin, and amphotericin), and incubated at 37 °C in a humidified atmosphere containing 5% CO_2 and 95% air.

2.7. MTT cytotoxicity assay

The standard MTT ["3-(4, 5-Dimethylthiazol-2-yl)-2, 5-diphenyl tetrazolium bromide"] assay was employed to evaluate the cytotoxic effects of Y_2O_3/AgO NCs. The IC50 values for the synthesized Y2O3/AgO NCs were ascertained using a cell viability curve. In 96-well plates, cells (1×10^4 to 1×10^6 cells mL^{-1}) were cultivated to a final volume of 200 µL of complete culture medium per well. The plates were covered with sterile parafilm, gently stirred, and incubated at 37 °C with 5% CO_2 for 24 hours. Following incubation, the medium was removed, and 200 µl of a 2-fold serial dilution of Y2O3/AgO NCs solutions (10, 25, 50, 100, 250, 500, 1000 µg ml−1) was introduced to the wells. Triplicate tests were conducted at each concentration and control. Each concentration and control was evaluated in triplicate. After the careful removal of the medium, each well was

replenished with 100 ml of DMSO solubilization solution and incubated for 5 minutes. The absorbance was measured at a wavelength of 550 nm using a Bio-Rad ELISA reader (Germany). The untreated control cells (100% cell viability) were utilized to represent the percentage of cell viability. The cell viability and cell inhibition percentages were calculated according to equations (1) and (2), respectively, [40,41]:

$$\text{Viability (\%)} = \frac{\text{optical density of sample}}{\text{optical density of control}} 100 \quad \ldots\ldots (1)$$

$$\text{Inhibition (\%)} = 100 - \text{Viability \%} \quad \ldots\ldots (2)$$

2.8. Statistical analysis

The study's findings were presented as the mean value ± standard error for three separate examinations. A one-way ANOVA and the Tukey HSD post hoc test were used for statistical analysis of the data. ORIGINLAB 2021 was used to create the graphs, while IBM SPSS was utilized for statistical analysis.

3. Results and discussion

3.1. X-Ray Diffraction (XRD) analysis.

The crystalline structure and phase composition of Y_2O_3/AgO NCs synthesized by a hybrid method were verified by XRD analysis. XRD patterns analysis showed 12 diffraction peaks at 2θ values ranging from 10° to 80° are shown in Figure 4, the appearance of several peaks indicates that the prepared sample is not a singular phase but a binary combination including yttrium oxide and a silver oxide phase. The peaks appear are at 19.634°, 29.718°,35.525°, 39.39°, 43.63°,46.49°, 53.97°,62.26°, and 70.65°, which corresponded to the Miller indices (211), (222),(411), (323), (431), (521),(220),(611),(701), and (732), respectively, set of Y_2O_3 lattice planes (cubic structure) and matched the (JCPDS card No. 41-1105). The diffraction peaks at 19.634°21.779°,, 24.433°, 29.718°, 32.538°, 39.49°, 43.75°, 46.49°, 53.97°,62.26°and 70.65° correspond to the monoclinic structure of crystalline AgO in the (100), (101), (110), (121), (202), (004), (114), (132), (231), (318), (220) and (302) planes, respectively, this matched the (JCPDS card No. 84-1108). We found that all Y_2O_3 and AgO diffraction peaks were quite near to and overlapped with one another. Also, all $_2O_3$/AgO NCs peaks shifted slightly lower. It is caused by Y_2O_3 atom diffusion into the AgO lattice structure [42].

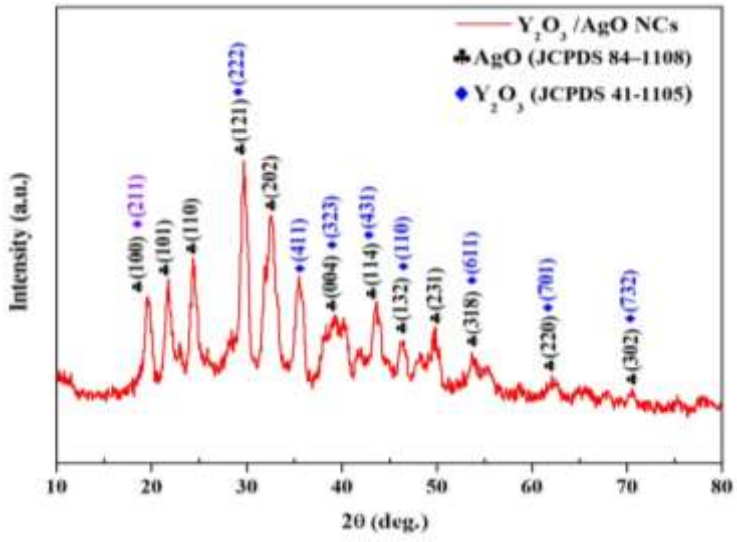

Fig. 4 XRD pattern of Y_2O_3/AgO NCs.

The crystallite size of the sample was calculated from the broadening of XRD peaks to determine the crystallite size of Y_2O_3/AgO NCs via the Debye-Scherrer equation [43]:

$$D = \frac{K\lambda}{\beta\cos(\theta)} \quad \ldots (3)$$

Where: *D* represents the average crystallite size. K is the Scherrer constant, which is approximately 0.9. λ is the wavelength of the X-ray radiation. β is the full width at half-maximum (FWHM) measured in radians. θ is the Bragg angle. According to Eq. (3), the average crystallite size of Y_2O_3/AgO NCs is found to be approximately 9.82 nm as reported in **Table 1**.

Table 1: XRD measurements of Y_2O_3/AgO NCs.

Material	Card No.	Phase	2θ°	FWHM (nm)	(hkl)	Crystallite size (nm)
Y_2O_3	JCPDS 41-1105	Cubic	19.634	0.78	211	10.36
			29.718	0.8	222	10.3
			35.525	0.82	411	10.2
			39.49	1.64	323	5.16
			43.75	0.9	431	9.53
			46.49	0.7	521	12.38
			49.8	0.96	220	9.14
			53.97	1.2	611	7.44
			62.26	1.2	701	7.75
			70.65	0.6	732	16.25
AgO	JCPDS 84-1108	monoclinic	19.634	0.78	100	10.36
			21.779	0.72	101	11.26
			24.433	0.77	110	10.58
			29.718	0.8	121	10.3
			32.538	1.14	202	7.28
			39.49	1.64	400	5.16
			43.75	0.9	114	9.53
			46.49	0.7	132	12.38
			49.8	0.96	231	9.14
			53.97	1.2	318	7.44
			62.26	1.2	220	7.75
			70.65	0.6	302	16.25
Average crystallite size						9.82

3.2. EDS and element mapping analysis.

The chemical composition of the produced Y_2O_3/AgO composite nanoparticles was analyzed by Energy Dispersive X-Ray Spectroscopy (EDS). Fig.5 illustrates that the EDS spectrum analysis identified the presence of Y, Ag, and O, confirming that the sample was successfully pure, with no impurity elements detected in Y_2O_3/AgO NCs. The weight percentages of Y, Ag, and O were 22.24%, 43.52%, and 34.24%, respectively. The atomic percentages of the compositions were 8.96% for Y, 14.44% for Ag, and 76.60% for O. Fig.4. show the elemental mapping revealed that silver, yttrium, and oxygen were uniformly distributed in Y_2O_3/AgO nanocomposites. In the merged map, Ag has increased brightness and importance, indicating a greater local concentration, whereas Y and O are more uniformly distributed. According to the XRD findings, along with the lack of extra elemental peaks

in the EDX spectra, confirm the successful synthesis of Y_2O_3/AgO nanocomposites via a plasma-assisted method using the peel extract.

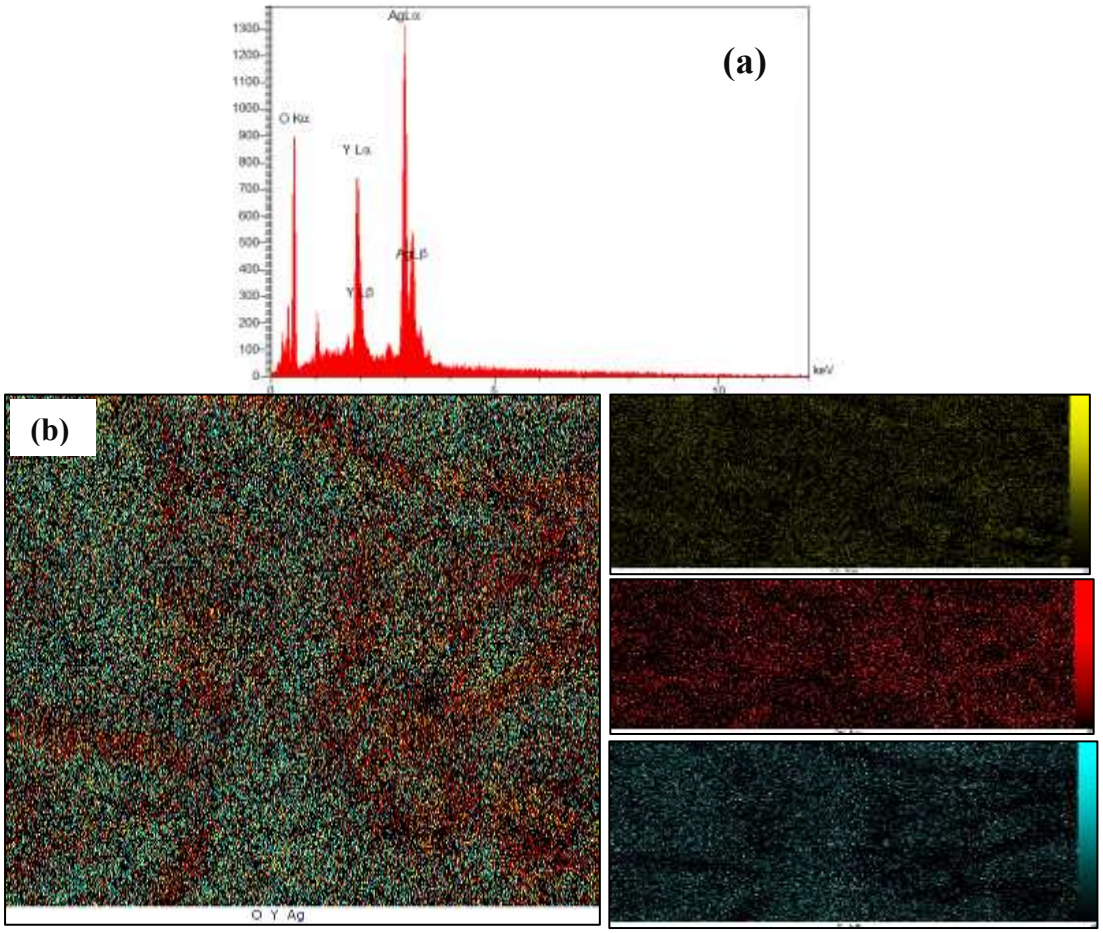

Fig. 5 (a): EDS of Y_2O_3/AgO NCs. **(b):** Element mapping.

3.3. FTIR spectra analysis.

The FT-IR spectrum of *Solanum Melongena L. peel* extract indicates the presence of anthocyanin molecules, exhibiting spectral characteristics aligned with nasunin, the predominant pigment in *Solanum Melongena L. peel*, as shown in Fig. 6. The broad absorption peak at 3420.3 cm^{-1} corresponds to the O–H stretching vibrations of phenolic groups and alcohols. The peak value at 2935.2 cm^{-1} is attributed to the asymmetric and symmetric C–H stretching vibrations of aliphatic methyl (CH_3) and methylene (CH_2) groups. The absorption at 1640.95 cm^{-1}, associated with carbonyle groups, signifies C=O stretching and C = C aromatic stretching vibrations, indicative of Phenolic and anthocyanin. An additional absorption peak at 1383.94 cm^{-1} is ascribed to C-H bending and symmetric COO- stretching. The peak at 1056.52 cm^{-1} is attributed to C–O-C stretching vibrations in glycosidic linkage [44,45].

The FT-IR spectrum of Y_2O_3/Ag_2O nanocomposite NPs is shown in Fig. 6. The broad band at 3437 cm^{-1} signifies the O–H stretching vibrations of hydroxyl groups associated with hydrogen-bonded alcohols and likely intramolecular hydrogen bonds from water molecules. The peaks at 2929.85, 2855.18, and 2765.96 cm^{-1} indicate C–H antisymmetric and symmetric stretching vibrations. The peak at 2427.40 cm^{-1} may indicate the presence of unsaturated CO_2 or C–H

on the surface. This indicates the presence of an organic surface that functions as a stabilizer, preventing aggregation. The peaks at 1632.02 cm^{-1} correspond to the bending structure of adsorbed water (H–O–H). The bands at 1384, 1271, and 1094 cm^{-1} correspond to OH, C=O, and C–O bending vibrations on the surface. This suggests that an increased number of surface functional groups serves as stabilizers, sufficient for what appears to be alkali or green rotation. In the light plasma spectrum, maxima were observed at 839.97, 618.04, and 473.57 cm^{-1}. The peak at 473.57 cm^{-1} corresponds to the Y–O vibration of yttrium oxide (Y_2O_3) [46,47]. The peak value at 618.04 cm^{-1} indicates the Ag–O vibration, suggesting the presence of silver oxide (AgO) [48,49] or a partial intercalation of Y_2O_3 and AgO. The peak at 839.97 cm^{-1} corresponds to M–O–M bridging vibrations, which means that Ag–O/Y–O nanostructures are forming an oxide network connecting them all. The results demonstrate the formation of stable nanoparticles, including yttrium and silver oxides, augmented by functionalized surface groups, which ensure the dispersion and stability of the particles.

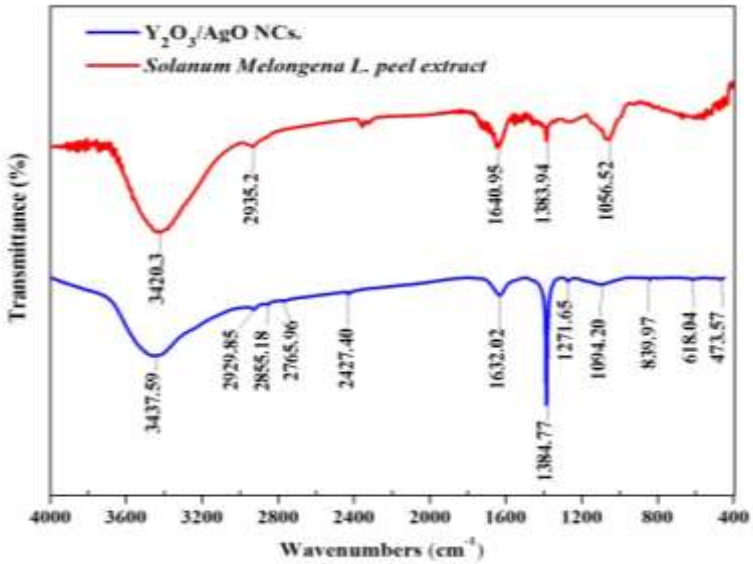

Fig.6 FT-IR spectra of Y_2O_3/AgO NCs and *Solanum Melongena L. peel* extract.

3.4. FE-SEM analysis.

The FE-SEM images of the Y_2O_3/AgO NCs are presented in Fig. 7. At different magnifications, the images present specific information about particle morphology, size distribution, and agglomeration extent. Monodispersed spherical shape with a limited size of nanoparticles on the particle surface is shown in FE-SEM images of Y2O3/AgO, and high dispersion is maintained. The particles have well-defined edges and a smooth surface, which implies a controlled growth mechanism and the synthesis of stable nanosized phases. The morphological surface of the sample possesses a fine and uniform texture due to interstitial nanosized spaces which could increase the effective surface area. This structure formation demonstrates the ability of synthesis conditions, under the control of biogenic constituents hosted into the extract and energy supplied by plasma, dictate particle generation while preventing related agglomeration phenomena thus realising a material with defined nanometric structure. FE-SEM morphologies reveal that the compound has a well-established, uniform and stable nanoscale surface suited for systems based on materials with enhanced surface area or activity.

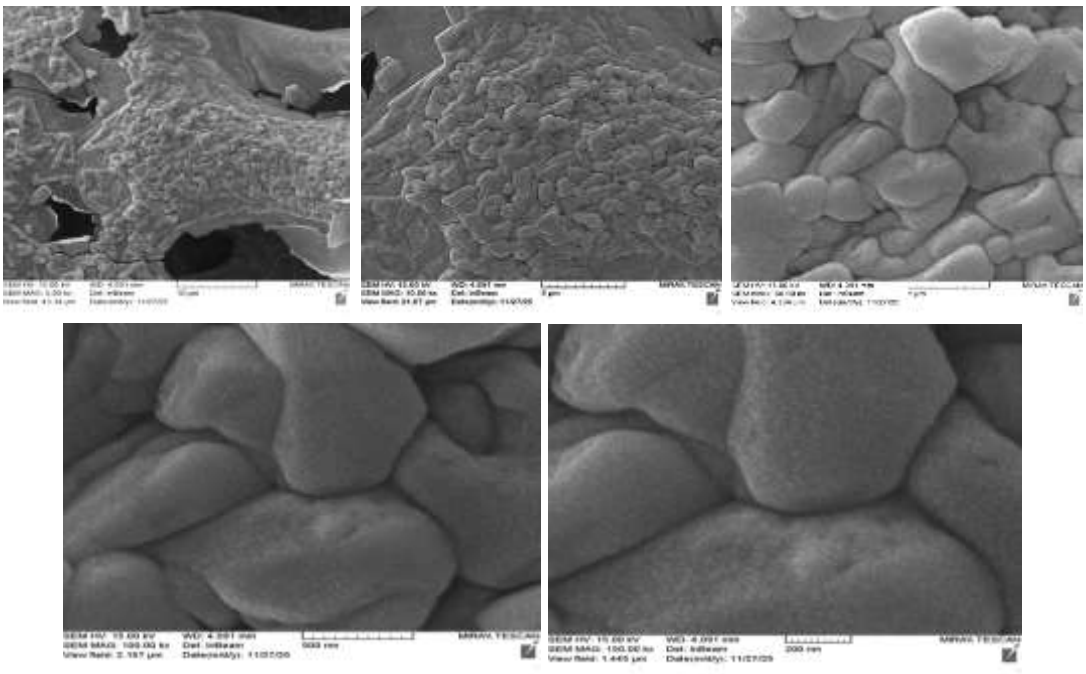

Fig.7 Surface morphology of Y_2O_3/AgO NCs at different scales.

3.5. TEM analysis

Transmission electron microscopy (TEM) images **in Fig. 8(a-e).** demonstrate Y_2O_3/AgO NCs synthesized via plasma solution interaction at magnifications of 300 nm, 100 nm, 50 nm, 20 nm, and 10 nm, respectively. The images demonstrate a difference in the distribution of these nanoparticles at varying magnification settings. At lower magnifications, black aggregates or clusters of nanoparticles are discerned. This phenomena frequently occurs in numerous nanomaterial research and is not regarded to be true agglomeration due to particle fusion; instead, it is typically ascribed to particles converging during the preparation process[50,51]. At higher magnifications, particularly at 10 nm, the images reveal uniformly distributed, spherical nanoparticles with near proximate nanometer dimensions. This verifies that the clusters seen at reduced magnifications signify secondary agglomeration, not genuine agglomeration. Prior research demonstrates that the use of an organic stabilizing or surface coating chemical significantly diminishes surface energy and inhibits interparticle adhesion, hence enhancing dispersion and preserving particle separation at higher magnifications. Consequently, the effective dispersion of these nanoparticles at high magnification serves as evidence of the efficient preparation procedure and the stability of the resultant nanocomposite[52]. The plasma jet production approach, along with the stabilizing action of the plant extract, likely facilitated a consistent particle size distribution and inhibited agglomeration.

The unique morphology of Y_2O_3/AgO NCs indicates their nanoscale separation, potentially improving the therapeutic efficiency of Y_2O_3/AgO NCs by enabling separate interaction with their target. Particle sizes were determined by analyzing transmission electron microscopy pictures with ImageJ software. The particle size chart **in Fig.9** indicates that the average size of the Y_2O_3/AgO nanoparticles is 3.7 ± 1.675 nm.

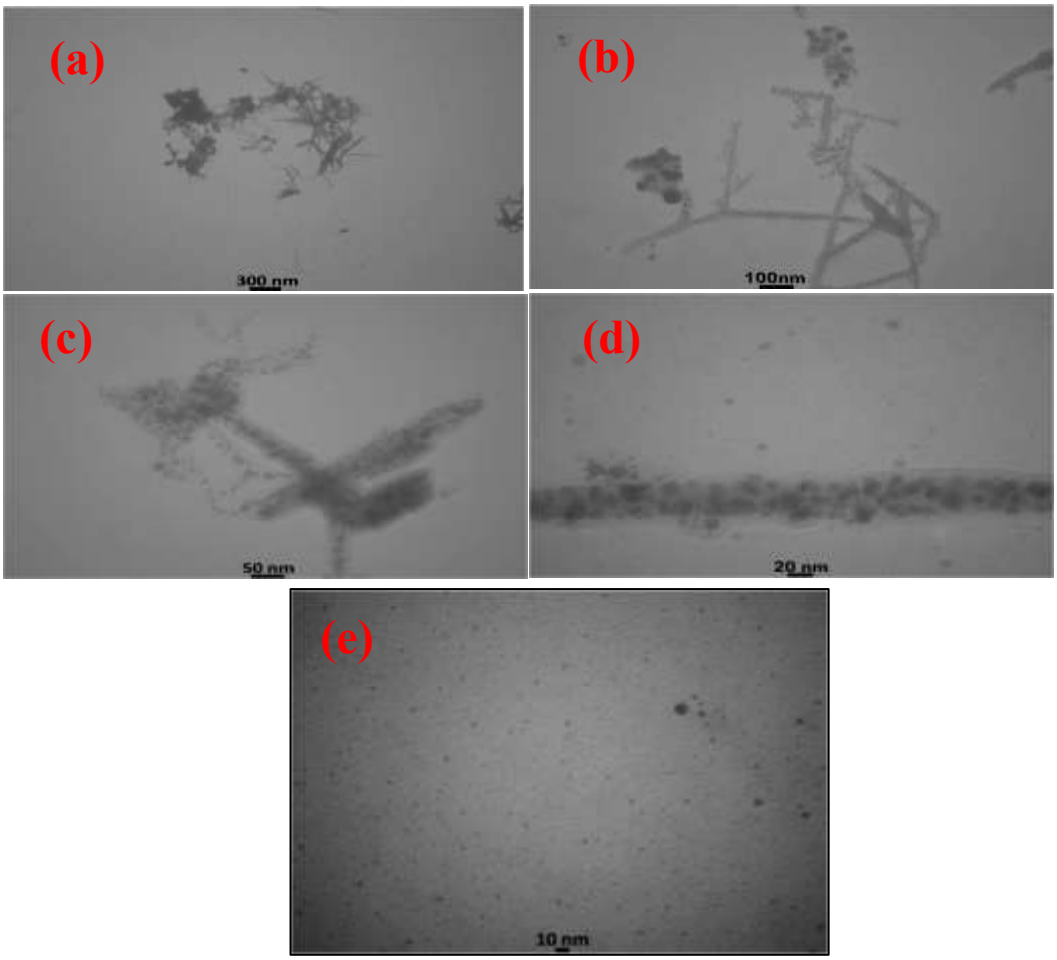

Fig. 8 TEM image of Y_2O_3/AgO NCs at a scale of different magnifications.

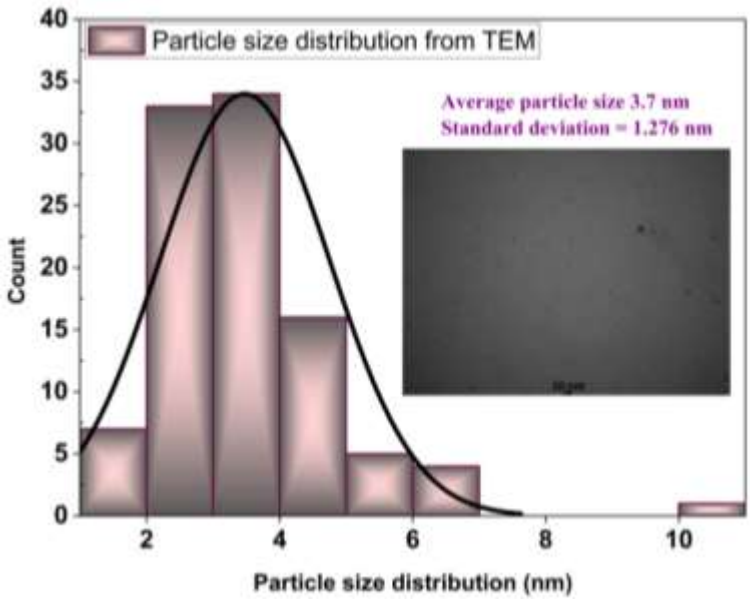

Fig.9 Size distribution histograms of Y_2O_3/AgO NCs.

3.6. UV−Visible spectra analysis.

Using UV–Vis spectrophotometry, the optical characteristics of the produced Y_2O_3/AgO nanocomposites were examined. The successful synthesis and optical activity of the generated NCs were confirmed by the absorbance spectra of the samples, which were recorded at 25°C in the wavelength range of 200–800 nm. As shown in Fig.10, the maximum absorption peak was seen in the wavelength region of 319 nm in the UV-Vis absorption spectra of Y_2O_3/AgO nanocomposites. Conduction and valence bands in metal oxide nanoparticles typically lie quite near to one another, making it simple for electrons to move between them. When free electrons are present on the surface of a nanoparticle, they collectively oscillate when they interact with incoming ultraviolet light, leading to the rise of Surface Plasmon Resonance (SPR) absorption. Through optical analysis, details on the physical characteristics of the nanoparticles, such as their bandgap energy and absorbance, were discovered. The bandgap energy is the most crucial component of optical properties. One popular method for figuring out the optical band gap energy of NPs is to plot the experimental absorbance data. The bandgap energy was measured directly from λ_{cut} using Planck's rule, which is displayed in Eq. (4):

$$E_g = \frac{hc}{\lambda} = \frac{1240}{\lambda} \ldots . (4)$$

Here, E_g is the energy gap, h is Planck's constant equal to 6.626×10^{-34} J.s, c is the light velocity (3×10^8 m/s), and λ is the wavelength that may be found by extending the linear portion of the absorption spectrum [53]. The optical bandgap energy (E_g) dropped when the absorption edge was redshifted or moved to longer wavelengths.

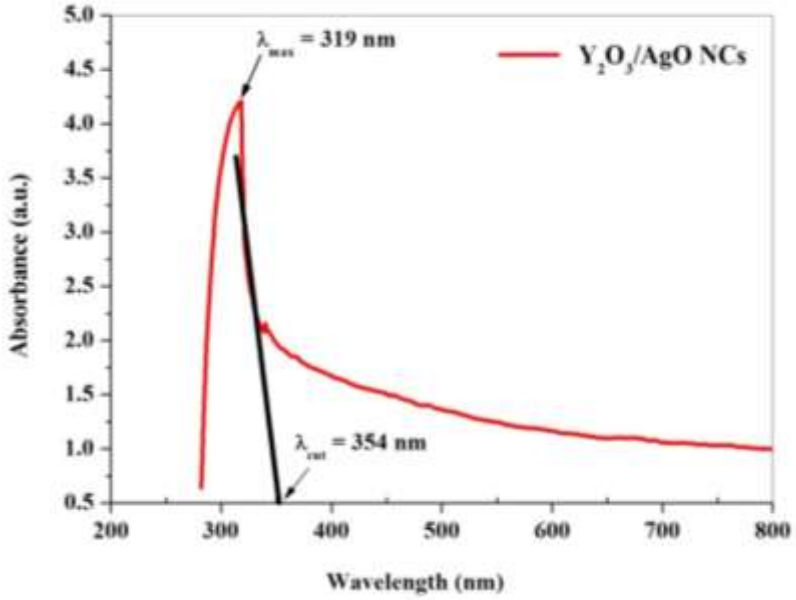

Fig. 10 UV–visible spectra of Y_2O_3/AgO NCs.

The absorption coefficients of the Y_2O_3/AgO nanoparticles were computed graphically using Tauc's relationship, Eq. (5), for direct transition:

$$(\alpha h\upsilon)^r = \mathrm{A}(\mathrm{h}\upsilon - E_g) \ldots\ldots (5)$$

A is a constant equal to 0.9, the band gap energy is E_g, the photon frequency is υ, the absorption coefficient is α, and r is the value of the direct transition (r =2). A popular method for calculating a band gap energy is shown in Fig.1 1, which uses the intercept of the extrapolated linear portion of the curve between the photon energy (hυ) and $(\alpha h\upsilon)^r$ with the x-axis. (4 eV) was the band gap energy.

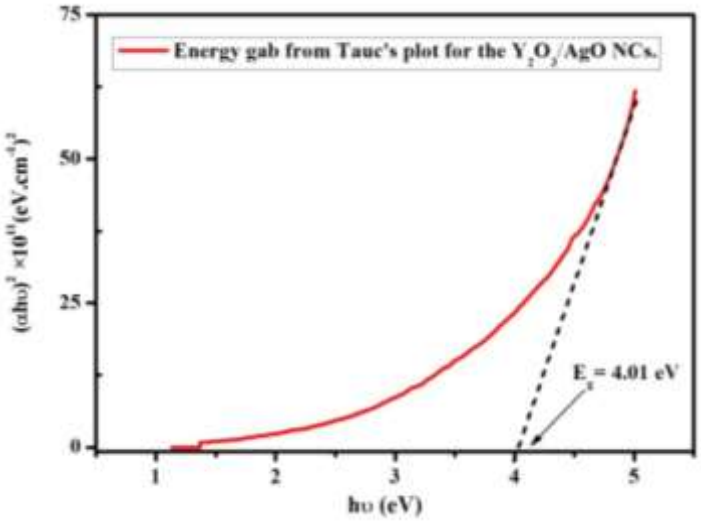

Fig. 11 Energy gap from Tauc's plot for the synthesized Y_2O_3/AgO NCs.

3.7. MTT Cytotoxicity

The cytotoxicity assessment of produced Y_2O_3/AgONCs was conducted in vitro via the MTT assay against human cancer cell lines, specifically follicular thyroid carcinoma (B-CPAP), alongside normal cells (Nthy-ori 3-1). For 24 hours, B-CPAP and Nthy-ori 3-1 cells (1×10^4 to 1×10^6 cells ml^{-1}) in each well were cultured with increasing concentrations of Y_2O_3/AgO NCs. Cell viability was determined as a percentage relative to the untreated control, which had been set at 100% viability. The results regarding the viability of cancer cells B-CPAP and Nthy-ori 3-1 normal cells following treatment with varying concentrations of Y_2O_3/AgO NCs (10, 25, 50, 100, 250, 500, and 1000 µg/ml) are listed in Table 2. The IC_{50} values were determined using the cell viability curve. The results show that the treatment with synthesized Y_2O_3/AgO NCs for 24 hours significantly inhibited B-CPAP cancer cell proliferation in a dose-dependent manner ($P < 0.0001$), resulting in a significant decrease in the survival rate of B-CPAP cells while exhibiting minimal cytotoxicity to Nthy-ori 3-1 normal cells. At a dosage of 10 µg ml^{-1}, no significant difference exists between B-CPAP cancer cells and Nthy-ori 3-1 normal cells. exhibits significant variations at higher doses ranging from 25 to 1000 µg ml^{-1}. The Y_2O_3/AgO NCs groups demonstrated a significant effect ($p < 0.0001$). At a dosage of 25 µg/ml, the viability of B-CPAP cancer cells decreased to 21.49758 % relative to the control group. The reduction continued, with cell viability stabilizing at a concentration of 50 µg $ml^{-1}$and higher, within the range of (6.88406-8.27295) %. The viability of Nthy-ori 3-1 normal cells decreased by approximately 59.7756 %. Cell viability decreased to 24.79663 % at a dose of 50 µg $ml^{-1}$and continued to decrease, stabilizing at concentrations of 100 µg/ml and higher within the range of (3.1136-3.73072) %. The maximum cytotoxicity was observed at a concentration of 250 µg ml^{-1}. For both B-CPAP cancer cells and

Nthy-ori 3-1 normal cell. The determined cytotoxicity (IC_{50}) for B-CPA cancer cells was 16.14 μg ml^{-1}. The assessed IC_{50} for normal cells was significantly elevated at 30.78 μg ml^{-1} as listed in **Table 2**.

Table 2: Viability of thyroid cancer and normal cells at different doses of Y_2O_3/AgO Ncs.

Dose concentrations (μg/mL)	Nthy-ori 3-1 cell line		B-CPAP thyroid cell line	
	Viability (Mean ± SD) (%)	Inhibition (%)	Viability (Mean ± SD) (%)	Inhibition (%)
0 (control)	100 ± 0.992	0	100 ± 7.174	0
10	100± 1.388	0	94.867 ±8.796****	5.1
25	59.776 ± 2.42****	40.2	21.498 ±0.342****	78.5
50	24.797 ± 1.745****	75.2	7.367 ± 0.171****	92.6
100	3.562 ± 0.278****	96.4	7.79 ± 0.427****	92.2
250	3.114 ± 0.278****	96.9	6.884 ± 0.171****	93.1
500	3.254 ± 0.079****	96.7	7.126 ± 0****	92.9
1000	3.731 ± 0.04****	96.3	8.273 ± 0.085 ****	91.7
IC50	30.78 μg/mL		16.14 μg/ml	

Notes: information of each dose presented as mean ± SD (n=3) and **** refer $P < 0.0001$ *vs* control.

According to MTT results, which were indicated in Fig. 12, Y_2O_3/AgO NCs had a practically lethal effect on B-CPAP cancer cells at certain concentrations, significantly less so on normal cells. This indicates a more significant response in cancer cells. At a dose of 25 μg ml^{-1}, the viability of cancer cells was less than that of normal cells at the identical concentration. At higher concentrations, cell viability diminished to levels similar for both cell types. This indicates the difference between them diminishes at higher concentrations, indicating a reduction in selectivity and the occurrence of toxic effects at high doses. Consequently, a concentration of 25 μg ml^{-1} was established as the best parameter for comparison assessment, as it exhibited the most significant differential effect between cancer B-CPAP cells and Nthy-ori 3-1 normal cells. Our conclusion indicates that the cytotoxicity of the produced Y_2O_3/AgO NCs in our investigation was dependent upon the cell type. The results indicate that synthesised Y_2O_3/AgO NCs have anticancer activities against thyroid cancer cells (B-CPAP cells) relative to normal cells, suggesting their potential as anticancer agents and requiring additional in vitro and in vivo investigations.

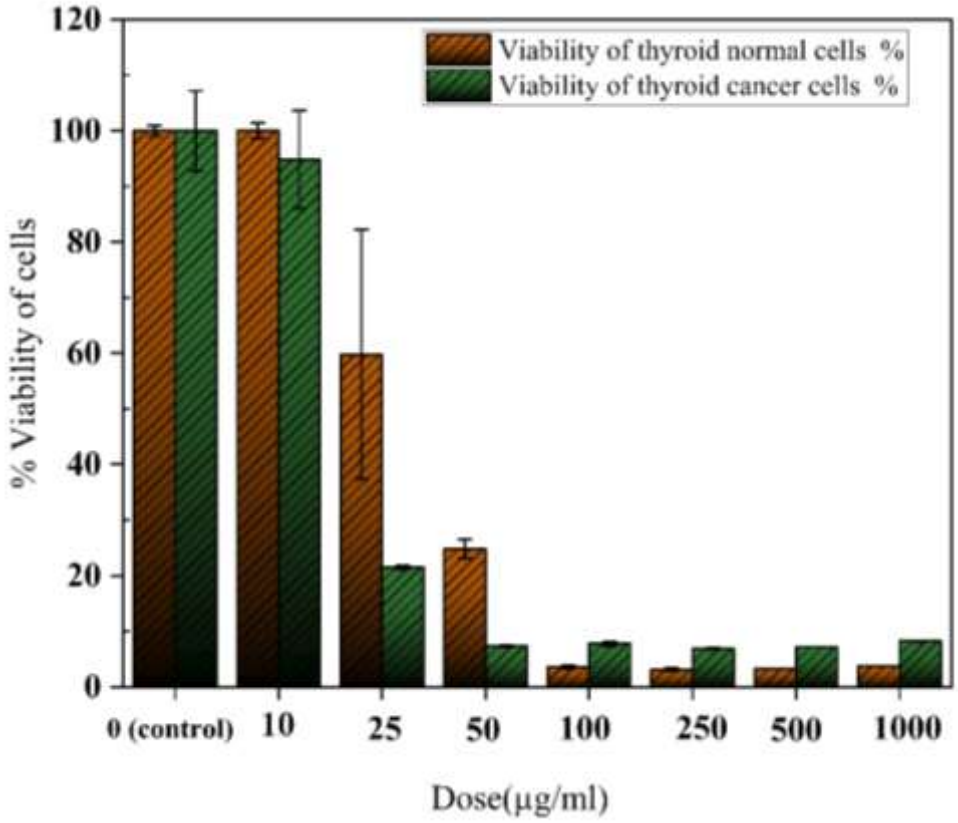

Fig. 12 % viability of Nthy-ori 3-1 and B-CPAP thyroid cell at different doses of Y_2O_3/AgO nanocomposite.

The toxic effects on Nthy-ori 3-1 normal and B-CPAP thyroid cancer cells can be evaluated 24 hours post-exposure to varying concentrations of Y_2O_3/AgO NCs by examining morphological alterations. The purple color represents intracellular formazan crystals formed by metabolically active cells. In Fig.13a, untreated normal cells demonstrated a healthy cell density typical of normal growth, but untreated cancer cells exhibited similar cell density without any morphological alterations, as illustrated in Figure 13a'. Exposure of cells to low concentrations of Y_2O_3/AgO NCs at 10 µg/ml resulted in a maintenance of structural integrity in normal cells, indicating biocompatibility at these concentrations, as illustrated in Fig.13b. Conversely, thyroid cancer cells demonstrated irregularity and a diminished intercellular cohesiveness, as illustrated in Fig.13b'. After exposure to a concentration of Y_2O_3/AgO NCs at 25 µg/ml, normal cells exhibited a comparatively better structural integrity, with a substantial number of cells staying intact and adherent, as illustrated in Fig.13c. Conversely, thyroid cancer cells exhibited significant toxicity, characterized by the dispersion of cellular debris, cellular disintegration, and a marked reduction in cell count, as depicted in Fig.13c′. Following exposure to a 50 µg/ml concentration of Y_2O_3/AgO NCs, normal cells demonstrated indications of cellular stress, characterized by reduced density and partial detachment, as illustrated in Fig.13d. In contrast, the morphological changes in cancer cells were more pronounced, characterized by a sharp decrease in their cellular structure and significant damage, near-complete loss of tissue cohesion, and the appearance of intercellular spaces, indicating a strong early cytotoxic effect of the nanoparticles in inducing cell death, as shown in Fig.13d′. Similarly, exposure of cells to a 100 µg/ml concentration of Y_2O_3/AgO NCs resulted in a significant cytotoxic effect in normal cells as showed in Fig.13e,

considered by notable morphological alterations and a substantial reduction in the number of healthy cells. The morphological alterations in cancer cells remained consistent with the previous concentration, signifying that the cytotoxic action had attained saturation, as illustrated in Fig.13e′.
At high levels of Y_2O_3/AgO NCs of (250, 500, and 1000) µg/ml, cancer cells exhibited a consistently low viability, with no substantial alterations compared to the preceding concentrations. This indicates that the cytotoxic effect remained stable at these high doses as illustrated in Fig.13 (f′-h′). Also, in normal cells as showed in Fig.13(f–h), significant degradation of the cell structure was observed, accompanied by damage and an almost total loss of viability.

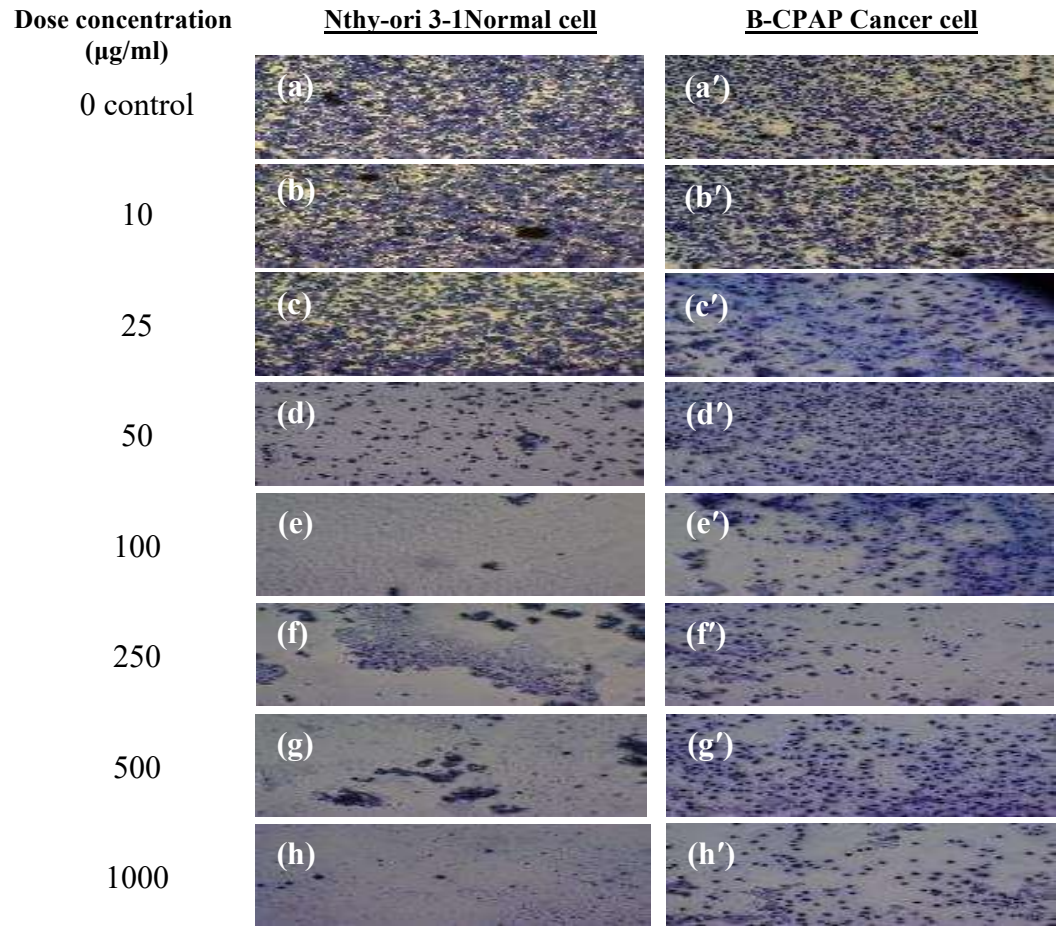

Fig. 13 Microscopic images of histological sections of thyroid cancer (B-CPA) and Nthy-ori 3-1 cell line at different concentrations of Y_2O_3/AgO nanocomposite.

Silver oxide nanoparticles (AgO NPs) may induce cancer cell apoptosis by generating reactive oxygen species (ROS) that inflict damage on cancer cells[54]. Research indicates that the anticancer properties of accessible silver oxide nanoparticles are attributed to the cellular damage they cause, resulting in the generation of reactive oxygen species (O•−, H_2O_2). Hydrogen peroxide (H_2O_2) and the superoxide anion (O•−) may induce apoptosis by influencing signaling pathways[55]. Moreover, elevated superoxide radical generation has been linked to heightened mitochondrial membrane potential and the disruption of cellular respiration. Certain

oncological pharmaceuticals function by producing superoxide radicals[56]. Current research indicate that silver oxide nanoparticles may promote the generation of reactive oxygen species (ROS), resulting in cellular damage and apoptosis. The initiation of programmed cell death is due to rising oxidative stress and the generation of reactive oxygen species (ROS). In cases of significant oxidative stress, when antioxidant defenses are exhausted, cytotoxicity may ensue, resulting in programmed cell death due to mitochondrial impairment and the release of apoptotic proteins. Additional observable indicators of harmful effects encompass membrane impairment, protein misfolding, and DNA destruction. Nanoparticles influence mitochondria, impairing their electron transport chain and resulting in heightened synthesis of superoxide dismutases (O2•−)[57]. Conversely, research indicates that Y2O3 nanoparticles possess antioxidant capabilities that modulate reactive oxygen species (ROS) levels and enhance their formation in cancer cells, resulting in genetic material damage, mitochondrial dysfunction, and the induction of apoptosis, while minimally affecting normal cells[58]. Thus, the amalgamation of Y_2O_3 and AgO into a singular nanocomposite induces oxidative stress within the cell due to the synergistic interaction of the two materials, as the Y_2O_3 matrix enhances particle stability and optimizes their engagement with cancer cells, thereby maintaining the selective toxic effect of AgO while preserving the compound's biological activity[59]. The surface charge of the Y_2O_3/AgO nanocomposite is essential to its cytotoxicity. The positively charged Ag+ and Y_3+ ions engage in electrostatic interactions with the negatively charged cancer cell membrane, thereby weakening it and enhancing its permeability. This interaction promotes the entrance of nanoparticles into the cell and amplifies the efflux of its contents, thereby enhancing the cytotoxic effect and heightening the cells' susceptibility to oxidative stress[60]. Prior research has demonstrated that the liberation of silver ions from silver oxide nanoparticles disturbs cellular enzymes and interferes with essential pathways related to cell survival, resulting in expedited cancer cell mortality[61]. The greater efficacy of the AgO/Y_2O_3 nanocomposite, in contrast to individual metal oxides, is ascribed to the synergistic interaction among reactive oxygen species formation, mitochondrial malfunction, cell membrane impairment, and the initiation of apoptosis. These mechanisms have been observed in prior research on Y_2O_3 and AgO-based nanocomposites[62–64]. The results of the current inquiry, which were generated from the transmission electron microscopy (TEM) examination, indicate that the nanoparticles of the Y_2O_3/AgO NCs have a small nanoscale size and a homogeneous distribution, which suggests that they have a greater effective surface area[65]. For this reason, their little size is a significant aspect that contributes to the enhancement of their contact with cells. Nanoparticles that are smaller in size have a greater surface area in comparison to their volume. This makes it simpler for them to engage with cells, pass through membranes, and be more poisonous and effective against cancer cells. Nanoparticles are able to penetrate malignant cells more easily as a result of their significantly reduced size[66]. There is a possibility that they will gather around the nucleus or the mitochondria, which will lead to a fatal malfunction in the cell. The size of particles influences their entry into cells and their processing within the endocytic pathway[67]. Research indicates that 2 nm DNA particles are significant against the 10 nm thickness of cell membranes. Moreover, 6 nm gold nanoparticles show increased nuclear internalization, while particles sized 10−16 nm primarily remain in the cytoplasm. Smaller particles offer a larger surface area-to-volume ratio, promoting self-aggregation and biological interactions, which may disrupt normal cellular functions [68].

4. Conclusion

This study utilised a novel, eco-friendly, and economical method to effectively synthesise Y_2O_3/AgO nanocomposites by integrating an extract of *Solanum melongena L.* peel, which served as a reducing and stabilising agent, with the plasma-liquid interaction technique. The XRD analysis indicated nanoparticles exhibiting a pure crystalline structure and a multiphase structure due to the presence of two distinct components with cubic and monoclinic geometries. The samples exhibited high purity, as verified by EDS results, indicating that silver, yttrium, and oxygen were the primary components. FTIR analysis identified unique functional groups, demonstrating that phenolic compounds, anthocyanins, carbonyls, and other plant constituents work as stabilising and coating agents in the nanoparticle manufacturing process. TEM and FE-SEM results verified that the Y_2O_3/AgO NCs were spherical, uniformly dispersed, and displayed minimal aggregation. The unique absorption peak at 319 nm was validated by UV-Vis absorption spectroscopy. Cytotoxicity assays on human B-CPAP thyroid cancer cells, in contrast to normal cells, revealed a significant dose-dependent reduction in cell viability. This compound demonstrates cytotoxic potential at low concentrations, signifying the anticancer efficacy of the Y_2O_3/AgO NCs manufactured by eco-friendly procedures. In conclusion, the present results indicate that the Y_2O_3/AgO NCs synthesised by eco-friendly procedures exhibit a stable crystalline structure and notable biological activity, making them interesting candidates for biomedical applications. Plant-based synthesis provides an integrated method for producing multifunctional nanomaterials. The utilization of a green synthesis method to combine an extract of *Solanum melongena L.* peel with a $Y(NO_3)_3$, and $AgNO_3$ solution subjected to plasma treatment is an innovative concept that remains undocumented in the existing research literature.

Acknowledgments

The author expresses thanks for the Mustansiriyah University (www.uomustansiriyah.edu.iq) Baghdad-Iraq for its support in the present work and assistance received from the Iraqi Center of Cancer Research and Medical Genetics for their support in providing cancer cell lines.

Authors Declaration

The authors declare that they have no known competing financial interests or personal relationships that could have appeared to influence the work reported in this paper.

Ethical Approval

None.

Funding: No funding was received to assist with the preparation of this manuscript.

Data availability: Data are available from the authors upon reasonable request.

Conflict of Interests

No conflict of interest among authors.

Competing interests: The authors have no relevant financial or non-financial interests to disclose.

Author contribution: Conceptualization, R.S.M. and R.S.A.; Methodology, R.S.M.; Data collection, R.S.M., R.S.A., and Y.Q.; formal analysis, Y.Q. and R.S.M.; Writing original draft manuscript, Y.Q.; review and editing, R.S.M. All authors have read and agreed to the published version of the manuscript.

Reference

[1] Matthews HK, Bertoli C, de Bruin RAM. Cell cycle control in cancer. Nat Rev Mol Cell Biol 2022;23:74–88. https://doi.org/10.1038/s41580-021-00404-3.

[2] Sung H, Ferlay J, Siegel RL, Laversanne M, Soerjomataram I, Jemal A, et al. Global Cancer Statistics 2020: GLOBOCAN Estimates of Incidence and Mortality Worldwide for 36 Cancers in 185 Countries. CA Cancer J Clin 2021;71:209–49. https://doi.org/10.3322/caac.21660.

[3] Bray F, Laversanne M, Sung H, Ferlay J, Siegel RL, Soerjomataram I, et al. Global cancer statistics 2022: GLOBOCAN estimates of incidence and mortality worldwide for 36 cancers in 185 countries. CA Cancer J Clin 2024;74:229–63. https://doi.org/10.3322/caac.21834.

[4] Fayadh SM, Mohammed AH. Silver nanoparticles induced apoptosis in papillary and follicular thyroid carcinoma cells. Phys Med 2022;14:100056. https://doi.org/10.1016/j.phmed.2022.100056.

[5] Lyu Z, Zhang Y, Sheng C, Huang Y, Zhang Q, Chen K. Global burden of thyroid cancer in 2022: Incidence and mortality estimates from GLOBOCAN. Chin Med J (Engl) 2024;137:2567–76. https://doi.org/10.1097/CM9.0000000000003284.

[6] Hosseinzadeh S, Nazari H, Esmaeili E, Hatamie S. Polyethylene glycol triggers the anti-cancer impact of curcumin nanoparticles in sw-1736 thyroid cancer cells. J Mater Sci Mater Med 2021;32:112. https://doi.org/10.1007/s10856-021-06593-9.

[7] Kim J, Gosnell JE, Roman SA. Geographic influences in the global rise of thyroid cancer. Nat Rev Endocrinol 2020;16:17–29. https://doi.org/10.1038/s41574-019-0263-x.

[8] Khan SU, Fatima K, Aisha S, Malik F. Unveiling the mechanisms and challenges of cancer drug resistance. Cell Commun Signal 2024;22:109. https://doi.org/10.1186/s12964-023-01302-1.

[9] Chehelgerdi M, Chehelgerdi M, Allela OQB, Pecho RDC, Jayasankar N, Rao DP, et al. Progressing nanotechnology to improve targeted cancer treatment: overcoming hurdles in its clinical implementation. Mol Cancer 2023;22:169. https://doi.org/10.1186/s12943-023-01865-0.

[10] Sengar A. The Role of Nanotechnology in Revolutionizing Cancer Treatment The Role of Nanotechnology in Revolutionizing 2025:0–6. https://doi.org/10.20944/preprints202503.0713.v1.

[11] Mi P. Stimuli-responsive nanocarriers for drug delivery, tumor imaging, therapy and theranostics. Theranostics 2020;10:4557–88. https://doi.org/10.7150/thno.38069.

[12] Venturini J, Chakraborty A, Baysal MA, Tsimberidou AM. Developments in nanotechnology approaches for the treatment of solid tumors. Exp Hematol Oncol 2025;14:76. https://doi.org/10.1186/s40164-025-00656-1.

[13] Asghar N, Hussain A, Nguyen DA, Ali S, Hussain I. Advancement in nanomaterials for environmental pollutants remediation : a systematic review on bibliometrics analysis , material types , synthesis pathways , and related mechanisms. J Nanobiotechnology 2024. https://doi.org/10.1186/s12951-023-02151-3.

[14] Ma X, Tian Y, Yang R, Wang H, Allahou LW, Chang J, et al. Nanotechnology in healthcare, and its safety and environmental risks. J Nanobiotechnology 2024;22:715. https://doi.org/10.1186/s12951-024-02901-x.

[15] Sun L, Liu H, Ye Y, Lei Y, Islam R, Tan S, et al. Smart nanoparticles for cancer therapy. Signal Transduct Target Ther 2023;8:418. https://doi.org/10.1038/s41392-023-01642-x.

[16] A Comprehensive Review of Nanomaterials: Types, Synthesis, Characterization, and Applications. Biointerface Res Appl Chem 2022;13:41. https://doi.org/10.33263/BRIAC131.041.

[17] Devan RS, Patil RA, Lin J, Ma Y. One-Dimensional Metal-Oxide Nanostructures: Recent Developments in Synthesis, Characterization, and Applications. Adv Funct Mater 2012;22:3326–70. https://doi.org/10.1002/adfm.201201008.

[18] Tunkaew K, Liewhiran C, Vaddhanaphuti CS. Functionalized metal oxide nanoparticles: A promising intervention against major health burden of diseases. Life Sci 2024;358:123154. https://doi.org/10.1016/j.lfs.2024.123154.

[19] Lin H, Liu Y, Deng J, Jing L, Wang Z, Wei L, et al. Bimetallic nanoparticles: advances in fundamental investigations and catalytic applications. Environ Sci Adv 2025;4:33–56. https://doi.org/10.1039/D4VA00241E.

[20] Sarfraz A, Usman M, Hussain N, Shafaat S, Khan AM, Hussain Z, et al. A Pathway to Optimal Multivariate Synthesis of Fe2O3-CuO Bimetal Oxide Hybrid Nanoparticles: Transformation Through Mathematical Modelling. JOM 2024;76:4179–98. https://doi.org/10.1007/s11837-024-06423-7.

[21] Redina EA, Kirichenko OA, Shesterkina AA, Kustov LM. Unusual behavior of bimetallic nanoparticles in catalytic processes of hydrogenation and selective oxidation. Pure Appl Chem 2020;92:989–1006. https://doi.org/10.1515/pac-2020-0207.

[22] Dawadi S, Katuwal S, Gupta A, Lamichhane U, Thapa R, Jaisi S, et al. Current Research on Silver Nanoparticles: Synthesis, Characterization, and Applications. J Nanomater 2021;2021:1–23. https://doi.org/10.1155/2021/6687290.

[23] Morozova O V. Silver Nanostructures: Limited Sensitivity of Detection, Toxicity and Anti-Inflammation Effects. Int J Mol Sci 2021;22:9928. https://doi.org/10.3390/ijms22189928.

[24] Kravanja KA, Finšgar M. A review of techniques for the application of bioactive coatings on metal-based implants to achieve controlled release of active ingredients. Mater Des 2022;217:110653. https://doi.org/10.1016/j.matdes.2022.110653.

[25] Li X, Liu X, Qian J, Zhang T, Sun B, Han Y. One-step synthesis and characterization of Y2O3 nanoparticles via emulsion detonation method. Ceram Int 2024;50:27995–8003. https://doi.org/10.1016/J.CERAMINT.2024.05.096.

[26] Rajakumar G, Mao L, Bao T, Wen W, Wang S, Gomathi T, et al. Yttrium oxide nanoparticle synthesis: An overview of methods of preparation and biomedical applications. Appl Sci 2021;11:1–24. https://doi.org/10.3390/app11052172.

[27] Kassem S, Arafa MM, Yehya MM, Soliman MAM. In vivo study of dose-dependent antioxidant efficacy of functionalized core–shell yttrium oxide nanoparticles. Naunyn Schmiedebergs Arch Pharmacol 2022;395:593–606. https://doi.org/10.1007/s00210-022-02219-1.

[28] Ali SQ, Kadhim DA, Mohammed AH, Mohammed RS, Abid MA, Athari SA. Green synthesis of α-MnO2/Ag nanocomposite using Malva parviflora (Khabbaz) extract for antimicrobial activity. Nano-Structures & Nano-Objects 2025;42:101467. https://doi.org/10.1016/j.nanoso.2025.101467.

[29] Talib WR, Sudhakaran A, Sudhakaran A, Mohammed RS. Potential biological and optoelectronic

applications of AgO:ZnO nanocomposite synthesized by green approach. Eur Phys J Plus 2024;139:1118. https://doi.org/10.1140/epjp/s13360-024-05920-7.

[30] Moradi F, Sedaghat S, Moradi O, Arab Salmanabadi S. Review on green nano-biosynthesis of silver nanoparticles and their biological activities: with an emphasis on medicinal plants. Inorg Nano-Metal Chem 2021;51:133–42. https://doi.org/10.1080/24701556.2020.1769662.

[31] Ali BMH, Almashhedy LAM. Green Synthesis Optimization and Characterization of Selenium Nanoparticle Using Aqueous Extract of Peel Solanum Melongena L. IOP Conf Ser Earth Environ Sci 2023;1158:102007. https://doi.org/10.1088/1755-1315/1158/10/102007.

[32] Balalakshmi C, Gopinath K, Govindarajan M, Lokesh R, Arumugam A, Alharbi NS, et al. Green synthesis of gold nanoparticles using a cheap Sphaeranthus indicus extract: Impact on plant cells and the aquatic crustacean Artemia nauplii. J Photochem Photobiol B Biol 2017;173:598–605. https://doi.org/10.1016/j.jphotobiol.2017.06.040.

[33] Jemilugba OT, Sakho EHM, Parani S, Mavumengwana V, Oluwafemi OS. Green synthesis of silver nanoparticles using Combretum erythrophyllum leaves and its antibacterial activities. Colloid Interface Sci Commun 2019;31:100191. https://doi.org/10.1016/j.colcom.2019.100191.

[34] Nyabadza A, McCarthy É, Makhesana M, Heidarinassab S, Plouze A, Vazquez M, et al. A review of physical, chemical and biological synthesis methods of bimetallic nanoparticles and applications in sensing, water treatment, biomedicine, catalysis and hydrogen storage. Adv Colloid Interface Sci 2023;321:103010. https://doi.org/10.1016/j.cis.2023.103010.

[35] Mohammed RS, Al -Marjani MF. Plasma–solution interaction as green pathway to synthesize novel hybrid nanoparticles for medical sterilization (catheter sterilization). Eur Phys J Plus 2025;140:156. https://doi.org/10.1140/epjp/s13360-025-06105-6.

[36] Ahmed RS, Mohammed RS, Abdul Majeed AM, Sudhakaran A. Biological activity of MgO nanoparticle synthesis by plasma-assisted reduction method. Phys Scr 2024;99:115901. https://doi.org/10.1088/1402-4896/ad7dbc.

[37] Kadhim DA, Mohammed RS, Abid MA, Sabry RS. Eco-friendly synthesis and plasma surface engineering of α-MnO2/AgO nanocomposite using Althaea officinalis extract for antimicrobial activity. Inorg Chem Commun 2025;182:115636. https://doi.org/10.1016/j.inoche.2025.115636.

[38] Pimklang T, Watthanaphanit A, Pakawatpanurut P. Novel green synthesis of graphene oxide-manganese dioxide using solution plasma process for energy storage. Chem Eng J 2022;442:136244. https://doi.org/10.1016/j.cej.2022.136244.

[39] Mohammed RS, Sudhakaran A, Mostafa MYA, Abbady G. Synthesize of ZnO and CuO nanoparticles with plasma jet at different treatment times and testing its optical parameters with UV-Vis-NIR. Appl Phys A 2024;130:533. https://doi.org/10.1007/s00339-024-07651-z.

[40] Feyadh SM, Mohammed AH. Syntheses, characterization, and suppression efficiency of silver & silver iodide nanoparticle for proliferation, migration, and invasion in follicular thyroid carcinoma cells. Mater Res Express 2022;9:055402. https://doi.org/10.1088/2053-1591/ac6d4b.

[41] Aly Khalil AM, Saied E, Mekky AE, Saleh AM, Al Zoubi OM, Hashem AH. Green biosynthesis of bimetallic selenium–gold nanoparticles using Pluchea indica leaves and their biological applications. Front Bioeng Biotechnol 2024;11. https://doi.org/10.3389/fbioe.2023.1294170.

[42] Ruffino F, Pugliara A, Carria E, Romano L, Bongiorno C, Spinella C, et al. Novel approach to the fabrication of Au/silica core–shell nanostructures based on nanosecond laser irradiation of thin Au films on Si. Nanotechnology 2012;23:045601. https://doi.org/10.1088/0957-4484/23/4/045601.

[43] Redjili S, Ghodbane H, Bourzami R, Mayouf F, Chebli D, Boudechicha A, et al. Green synthesis of silver oxide nanoparticles: Eco-friendly approach for sustainable solutions. Ind Crops Prod 2025;223:120168. https://doi.org/10.1016/j.indcrop.2024.120168.

[44] Hamaamin OK, Ghareeb HO, Mohammed SJ. Eco-friendly enhancement of optical and structural properties in polyvinyl alcohol films via eggplant peel dye doping. Sci Rep 2025;15:28891. https://doi.org/10.1038/s41598-025-14206-6.

[45] Imani NAC, Kusumaningtyas RD, Wijayanti DGS, Diyanti E, Auralita KP, Wikandaru A, et al. EVALUATING THE EFFICACY OF ENCAPSULATED-EGGPLANT PEEL EXTRACT AS A POTENTIAL ANTIOXIDANT SUPPLEMENT. ASEAN Eng J 2025;15:119–24. https://doi.org/10.11113/aej.v15.23154.

[46] Lin L, Starostin SA, Li S, Khan SA, Hessel V. Synthesis of yttrium oxide nanoparticles via a facile microplasma-assisted process. Chem Eng Sci 2018;178:157–66. https://doi.org/10.1016/j.ces.2017.12.041.

[47] Govindasamy R, Govindarasu M, Alharthi SS, Mani P, Bernaurdshaw N, Gomathi T, et al. Sustainable Green Synthesis of Yttrium Oxide (Y2O3) Nanoparticles Using Lantana camara Leaf Extracts: Physicochemical Characterization, Photocatalytic Degradation, Antibacterial, and Anticancer Potency. Nanomaterials 2022;12:2393. https://doi.org/10.3390/nano12142393.

[48] Elyamny S, Eltarahony M, Abu-Serie M, Nabil MM, Kashyout AE-HB. One-pot fabrication of Ag @Ag2O core–shell nanostructures for biosafe antimicrobial and antibiofilm applications. Sci Rep 2021;11:22543. https://doi.org/10.1038/s41598-021-01687-4.

[49] Abbasi BA, Iqbal J, Nasir JA, Zahra SA, Shahbaz A, Uddin S, et al. Environmentally friendly green approach for the fabrication of silver oxide nanoparticles: Characterization and diverse biomedical applications. Microsc Res Tech 2020;83:1308–20. https://doi.org/10.1002/jemt.23522.

[50] Johnson L, Gray DM, Niezabitowska E, McDonald TO. Multi-stimuli-responsive aggregation of nanoparticles driven by the manipulation of colloidal stability. Nanoscale 2021;13:7879–96. https://doi.org/10.1039/D1NR01190A.

[51] Fang T, Zhang Y, Yan Y, Dai C, Zhang J. Molecular insight into the aggregation and dispersion behavior of modified nanoparticles. J Pet Sci Eng 2020;191:107193. https://doi.org/10.1016/j.petrol.2020.107193.

[52] Javed R, Zia M, Naz S, Aisida SO, Ain N ul, Ao Q. Role of capping agents in the application of nanoparticles in biomedicine and environmental remediation: recent trends and future prospects. J Nanobiotechnology 2020;18:172. https://doi.org/10.1186/s12951-020-00704-4.

[53] Abbas BH, Abdalameer NK, Mohammed RS. Synthesis of Copper Oxide Nanostructures by Ar Plasma Jet and Study of Their Structural and Optical Properties. Iraqi J Sci 2024:1999–2006. https://doi.org/10.24996/ijs.2024.65.4.18.

[54] Al-Alawi MTK. Anti-Cancer Efficacy of Silver Oxide Nanoparticles Synthesized Using Terephthalic Acid: A Comprehensive Study. Hilla Univ Coll J Med Sci 2024;2:52–6. https://doi.org/10.62445/2958-4515.1038.

[55] Mukherjee S, Chowdhury D, Kotcherlakota R, Patra S, B V, Bhadra MP, et al. Potential Theranostics Application of Bio-Synthesized Silver Nanoparticles (4-in-1 System). Theranostics 2014;4:316–35. https://doi.org/10.7150/thno.7819.

[56] Ovais M, Hoque MZ, Khalil AT, Ayaz M, Ahmad I. Mechanisms underlying the anticancer applications of biosynthesized nanoparticles. Biog. Nanoparticles Cancer Theranostics, Elsevier; 2021, p. 229–48. https://doi.org/10.1016/B978-0-12-821467-1.00006-9.

[57] Nel A, Xia T, Mädler L, Li N. Toxic Potential of Materials at the Nanolevel. Science (80-) 2006;311:622–7. https://doi.org/10.1126/science.1114397.

[58] Chandra Das R, Chaki B ML, Sluyter R, Lerch M, Konstantinov K. Y2O3 nanoparticles with 2D morphology as reactive oxygen species scavengers under ultraviolet radiation conditions. Mater Lett 2023;346:134523. https://doi.org/10.1016/j.matlet.2023.134523.

[59] Nachimuthu S, Thangamani C, Thiyagarajulu N, Thangaraj K, Paramasivam D, Thangavel S, et al. Facile synthesis of ZnO-Y2O3 nanocomposite for photocatalytic and biological applications. Catal Commun 2023;184:106786. https://doi.org/10.1016/j.catcom.2023.106786.

[60] Pandiyan N, Murugesan B, Arumugam M, Chinnaalagu D, Samayanan S, Mahalingam S. Ionic liquid mediated green synthesis of Ag-Au/Y2O3 nanoparticles using leaves extracts of Justicia adhatoda: Structural characterization and its biological applications. Adv Powder Technol 2021;32:2213–25. https://doi.org/10.1016/j.apt.2021.04.030.

[61] Shah A, Sun H, Qiao Z, Umair Khan M, Ali N, Gao C, et al. Synthesis of Iron Oxide Nanoparticles and its Antimicrobial, Anticancer, Anti-inflammatory, Wound Healing, and Immunomodulatory Activities -A Review. Phytopharm Res J 2024;3:1–28.

[62] Chen Z, Han F, Du Y, Shi H, Zhou W. Hypoxic microenvironment in cancer: molecular mechanisms and therapeutic interventions. Signal Transduct Target Ther 2023;8:70. https://doi.org/10.1038/s41392-023-01332-8.

[63] Porosnicu I, Butnaru CM, Tiseanu I, Stancu E, Munteanu CVA, Bita BI, et al. Y2O3 Nanoparticles and X-ray Radiation-Induced Effects in Melanoma Cells. Molecules 2021;26:3403. https://doi.org/10.3390/molecules26113403.

[64] Poojari P, Mirjankar M, Gaddigal A, Shivappa P, Ganeshkar M, Huyilagola P, et al. Diverse approach for the evaluation of antibacterial, antioxidant, and cytotoxicity properties: Plant-mediated synthesis of AgO, ZnO and AgO-ZnO bimetallic nanoparticles using Theobroma cacao leaf extract. Next Nanotechnol 2025;8:100211. https://doi.org/10.1016/j.nxnano.2025.100211.

[65] Adamo G, Campora S, Ghersi G. Functionalization of nanoparticles in specific targeting and mechanism release. Nanostructures Nov. Ther., Elsevier; 2017, p. 57–80. https://doi.org/10.1016/B978-0-323-46142-9.00003-7.

[66] Gliga AR, Skoglund S, Odnevall Wallinder I, Fadeel B, Karlsson HL. Size-dependent cytotoxicity of silver nanoparticles in human lung cells: the role of cellular uptake, agglomeration and Ag release. Part Fibre Toxicol 2014;11:11. https://doi.org/10.1186/1743-8977-11-11.

[67] Shang L, Nienhaus K, Nienhaus GU. Engineered nanoparticles interacting with cells: size matters. J Nanobiotechnology 2014;12:5. https://doi.org/10.1186/1477-3155-12-5.

[68] Manuja A, Kumar B, Kumar R, Chhabra D, Ghosh M, Manuja M, et al. Metal/metal oxide nanoparticles:

Toxicity concerns associated with their physical state and remediation for biomedical applications. Toxicol Reports 2021;8:1970–8. https://doi.org/10.1016/j.toxrep.2021.11.020.